Supporting Information

Molecular Doping of the Hole-Transporting Layer for Efficient, Single-Step Deposited Colloidal Quantum Dot Photovoltaics

Ahmad R. Kirmani[1], F. Pelayo García de Arquer[2], James Z. Fan[2], Jafar I. Khan[1], Grant Walters[2], Sjoerd Hoogland[2], Nimer Wehbe[1], Marcel M. Said[3], Stephen Barlow[3], Frédéric Laquai[1], Seth R. Marder[3], Edward H. Sargent[2], and Aram Amassian[1,]*

[1]King Abdullah University of Science and Technology (KAUST), KAUST Solar Center (KSC), and, Physical Science and Engineering Division, Thuwal, 23955-6900, Saudi Arabia

[2]Department of Electrical and Computer Engineering, University of Toronto, Toronto, Ontario M5S 3G4, Canada.

[3]School of Chemistry and Biochemistry and Center for Organic Photonics and Electronics, Georgia Institute of Technology, 901 Atlantic Drive, Atlanta, GA, 30332-0400, United States

EXPERIMENTAL METHODS

CQD synthesis and solution-phase ligand exchange recipes. The initial OA-capped CQDs were synthesized following a reported recipe.[1]

Synthesis of perovskite-shelled PbS CQDs was carried out according to the reported protocol.[2] Equal amounts of MAI and PbI_2 precursors (0.3 $mol.L^{-1}$) were mixed in 5 mL of dimethylformamide (DMF) solvent at room temperature. Once a clear solution was obtained, *ca.* 5 ml of OA-capped PbS CQDs (10 mg mL^{-1}) were added and the vial was vortexed for 5 min. This resulted in solution-phase ligand exchange CQDs which were washed twice with octane (5 mL) to remove the residual OA ligands, separated from the vial, precipitated with toluene solvent (2.5 mL) and centrifuged at 6000 rpm for a couple of minutes. The precipitate thus obtained was dried under vacuum for 1 hour. This was then redispersed in butylamine solvent yielding a stable ink of desired concentration.

Synthesis of metal halide ligand capped PbS CQDs followed a recent report.[3] A clear solution of the precursors (0.1 M PbI_2, 0.02 M $PbBr_2$, 0.04 M ammonium acetate) was first made in 5 ml DMF solvent. 5 ml of OA-capped PbS CQDs (10 mg mL^{-1}) were then added to the vial and vortexed for 5 min. The resulting solution-phase ligand exchanged CQDs were washed thrice with octane. These were then precipitated with toluene and separated by centrifugation (6000 rpm, 2 min) and left under vacuum for drying for 1 hour. The powder was then redispersed in butylamine to obtain a stable ink of desired concentration.

Dopant synthesis. The metal-organic complex, Mo(tfd-$COCF_3$)$_3$ used as a p-dopant was prepared according to literature.[4]

Secondary Ion Mass Spectrometry (SIMS). SIMS experiments were performed on a Dynamic SIMS instrument from Hiden analytical company (Warrington-UK) operated under ultra-high vacuum conditions, typically 10^{-9} Torr. The Dynamic SIMS is equipped with a gas source allowing for both argon or oxygen ion beams to be employed. However, in order to reduce the fragmentation effect leading to the formation of small hydrocarbon fragments, the inert Ar^+ beam was chosen to conduct the measurements. In addition, the effect of the incoming oxygen on the sputtered organic material is also avoided.

Throughout the sputtering process, the selected ions ascribed C, F, Si, S, I, Mo and Pb were sequentially collected using a MAXIM spectrometer equipped with a quadrupole analyser. Ions are collected from the sample by a shaped extraction field and energy filtered using a parallel plate system, with the energy resolution matched to that of the quadrupole analyser. After passing through a triple filter system, detected ions are measured using a pulse counting detector having a 4 keV post acceleration potential to increase further the detection efficiency at high masses.

Prior to acquiring mass spectra and depth profiling curves, the experimental conditions including the primary ion type, energy and current of the sputtering beam were first optimized. The raster of the sputtered area is estimated to be 500 × 500 μm^2. In order to avoid the edge effect during depth profiling experiments, it is necessary to acquire data from a small area located in the middle of the eroded region. Using an adequate electronic gating, the acquisition area from which the depth profiling data were extracted was approximately 50 × 50 μm^2. The

conversion of the sputtering time to sputtering depth scale was carried out by measuring the depth of the crater generated at the end of the depth profiling experiment using a stylus profiler from Veeco.

Device fabrication. Reported device fabrication protocol was followed.[2] The active layer was directly deposited by spin-coating 40uL of the solution-phase exchanged CQD ink (160 uL solution in butaylamine solvent) at 6000 rpm. The $MAPbI_3$-PbS CQD layer was annealed at 70 °C in a nitrogen glove box. No post-annealing was required for the PbX_2-PbS CQD layer. The resulting single-step deposited absorber layers were found to be of high quality; thick, dark brown and shiny without any pinholes. This was followed by deposition of two layers of EDT-PbS QD via solid-state ligand exchange, in a layer-by-layer fashion. To obtain doped solar cells, the overall assembly was soaked in the dopant solution of a particular concentration for ~30 seconds. This was followed by an ACN wash to remove any excess dopant. 120 nm gold was finally deposited via thermal evaporation as the top electrode.

J – V characterization. *J–V* characterization was performed using a Keithley 2400 source-meter at ambient temperature. During the measurements, the solar cell was in a constantly purged nitrogen environment. The solar spectrum at AM1.5 was simulated to within class A specifications (less than 25% spectral mismatch) with a xenon lamp and filters (ScienceTech; measured intensity of 100 mW cm^{-2}). The aperture area was 0.049 cm^2.

EQE measurements. External-quantum-efficiency spectral traces were taken by illuminating the cells with a 400W Xe lamp passed through a monochromator and appropriate cutoff filters. The monochromator output power was calibrated with Newport 818-UV and Newport 838-IR photodetectors. The light beam was chopped at a 220 Hz frequency and focused in the pixel alongside 1 sun intensity light bias from a solar-simulator. The photoresponse of the cell was

recorded through a Lakeshore preamplifier connected to Stanford Research 830 lock-in amplifier at short-circuit conditions (virtual-null).

X-ray Photoelectron Spectroscopy. XPS was carried out in an ultrahigh vacuum (UHV) Omicron chamber equipped with a SPHERA U7 hemispherical energy analyzer, employing X-ray photons having an incident kinetic energy of 1486.6 eV from a monochromated Al K α X-ray source with a total energy resolution of 0.1 eV. The chamber base pressure for these measurements was $< 5 \times 10^{-9}$ mbar.

Ultra-violet Photoelectron Spectroscopy. UPS measurements were done under UHV base pressures of $< 8 \times 10^{-9}$ mbar. The photon line width was *ca.* 250 eV and the minimum spot size *ca.* 1 mm. He I photons (21.2 eV) were used to acquire the spectra at normal emission. The photoelectrons were collected by the SPHERA U7 hemispherical energy analyzer with a 7 channel MCD detector, in Constant Analyzer Energy (CAE) mode.

Kelvin-probe measurements. A KP Technology KP020 system was used to obtain the surface potential of the samples. A gold polished plate was used as a standard reference. Measurements were taken at ambient conditions with an off-null configuration.

Transient Absorption and Photoluminescence measurements. Transient absorption measurements were done using femtosecond pulses were produced from a Light Conversion Pharos regeneratively amplified Yb:KGW laser at a repetition rate of 5 kHz. The 440 nm pump signal was produced from a portion of the 1030 nm probe light with a Light Conversion Orpheus optical parametric amplifier. A Helios Ultrafast optical bench received the pump and probe beams where the probe light generated a near-IR continuum with a crystal from Ultrafast. The probe signal was optically delayed to introduce time delay. Alternating pump pulses were

blocked with a chopper. A charge-coupled device measure the transmitted probe after being collected and dispersed with a grating spectrometer. A pump pulse intensity of 6 $\mu J/cm^2$ was used in all measurements and the samples were translated during measurement. Photoluminescence measurements were done using a Horiba Fluorolog system. Light from a monochromatized xenon lamp was used as the photoexcitation source. Photoluminescence was collected by a single grating spectrometer and measured with a photo-multiplier tube detector.

Time-resolved Photoluminescence measurements. Time resolved photoluminescence (TRPL) measurements were conducted by applying an optical parametric oscillator (OPO) from Radiantis pumped by a Spectra Physics Maitai oscillator. The desired output of 650 nm from the OPO was routed through the pulse picker (Pulse Select from A.P.E) and focused to pump the quantum dot samples. The associated PL signal is then collected and focused through optical lenses to the slit entrance of the spectrograph and carried to the Infrared streak camera (Hamamatsu), and finally the detected signal is analyzed and optimized on a computer. All measurements were performed at room temperature.

Optoelectronic simulations. Optoelectronic simulations were performed with SCAPS.[5] The solar cell structure were modeled based on a p-i-n structure. The p-layer represents the modified EDT, the i-layer the perovskite-shelled quantum dots and the n-layer the ZnO. The acceptor doping concentration of the EDT layer was varied and analyzed for its impact on the various photovoltaic performance metrics.

The perovskite-shelled CQD layer consists of a parabolic grading combination of the parameters listed herein. The CQD band-edge for a given exciton peak was calculated from the absorption edge of the exciton peak. The parameters in bold were swept simultaneously.

	HTL	Perovskite-shelled CQD layer (power-law graded)	ZnO layer
Thickness (nm)	20	200	40
Bandgap edge (eV)	1.02	1.02	3.2
Electron affinity (eV)	3.9	4	4.3
Permittivity (Fm^{-1})	22	35	66
CB/VB DOS (cm^{-3})	10^{19}	10^{19}	$5 \cdot 10^{19}$
Electron mobility ($cm^2V^{-1}s^{-1}$)	$1 \cdot 10^{-2}$	$1 \cdot 10^{-2}$	$5 \cdot 10^{-2}$
N_{donor} (cm^{-3})	-	10^{17}	10^{16}
$N_{acceptor}$ (cm^{-3})	Swept	-	0
Capture cross section (cm^2)	$1.2 \cdot 10^{-13}$	$1.2 \cdot 10^{-13}$	
Position below Ec (eV)	0.3	0.3	
Density (cm^{-3})	10^{16}	10^{15}	
CQD-ZnO interface defects (neutral)			
Capture cross section (cm^2)		10^{-17}	
Position above Ev (eV)		0.6	
Density (cm^{-3})		$4 \cdot 10^{15}$	

For the band energy alignment calculations shown in Figure 3, N_{donor} in the HTL was set to 0 and $N_{acceptor}$ varied for the undoped (10^{15} cm^{-3}) and doped (10^{17} cm^{-3}) cases.

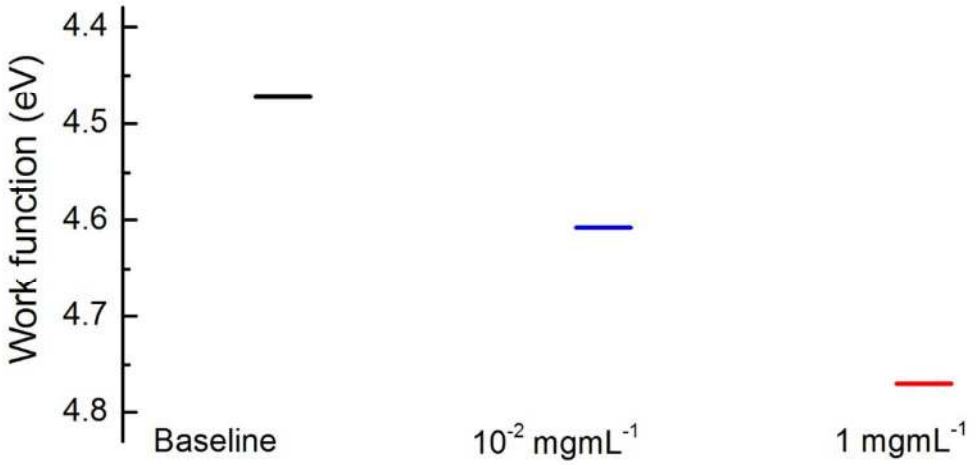

Figure S1. KP data for the various doping scenarios. The work function of the CQD solids is found to exhibit an increasing trend with doping concentration.

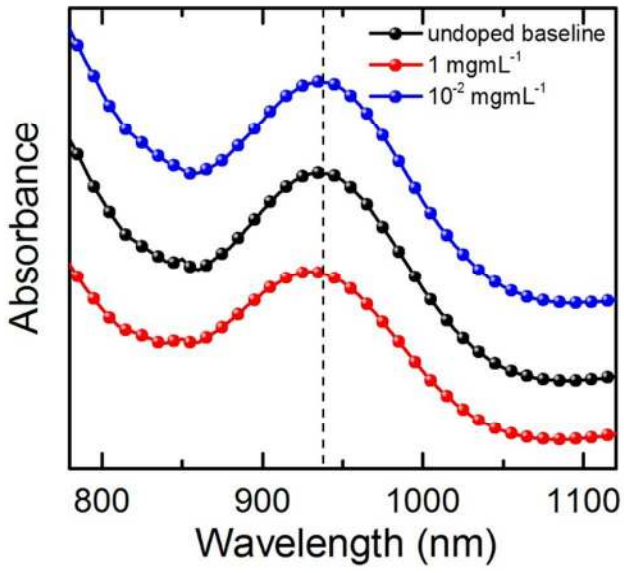

Figure S2. Steady-state absorption spectra for the various doping scenarios are shown with off-sets. No change in optical band gap is found after doping.

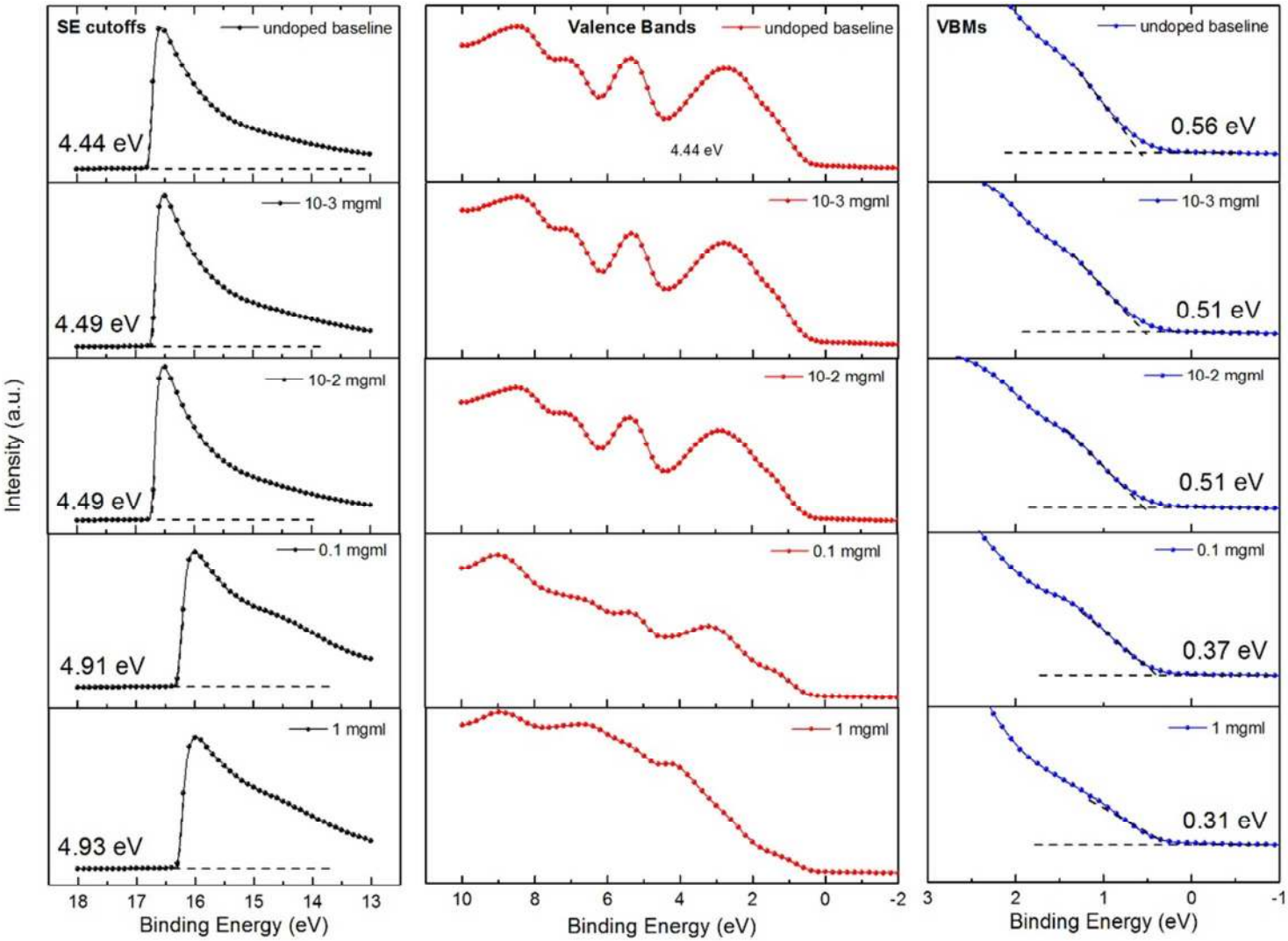

Figure S3. *UPS data.* Secondary electron cutoffs (black), valence bands (red) and valence band maxima (blue) for the various cases are shown.

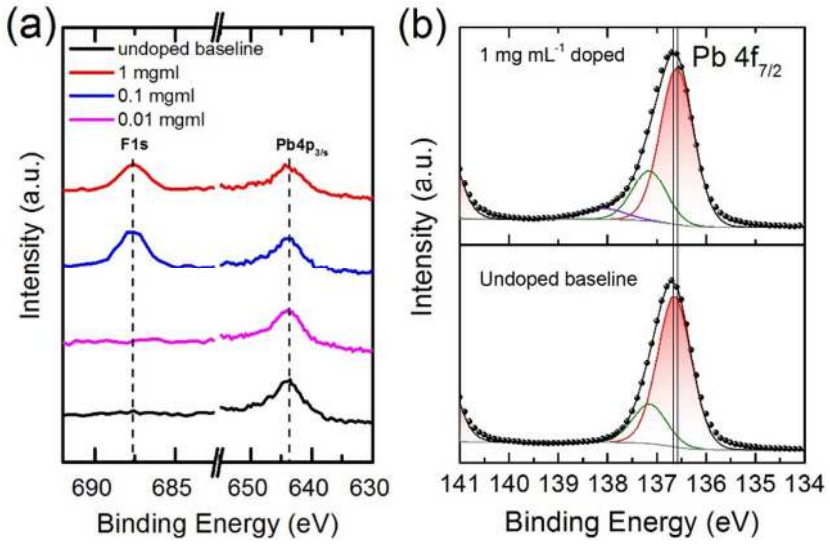

Figure S4. *XPS data.* (a) As the doping concentration is increased, the F1s core peak from the dopant increases in intensity as compared to the Pb $4p_{3/2}$ peak. (b) High resolution XPS of the Pb $4f_{7/2}$ peaks shows that the core level shifts to lower binding energy for the doped case, commensurate with the ΔE_F observed from UPS.

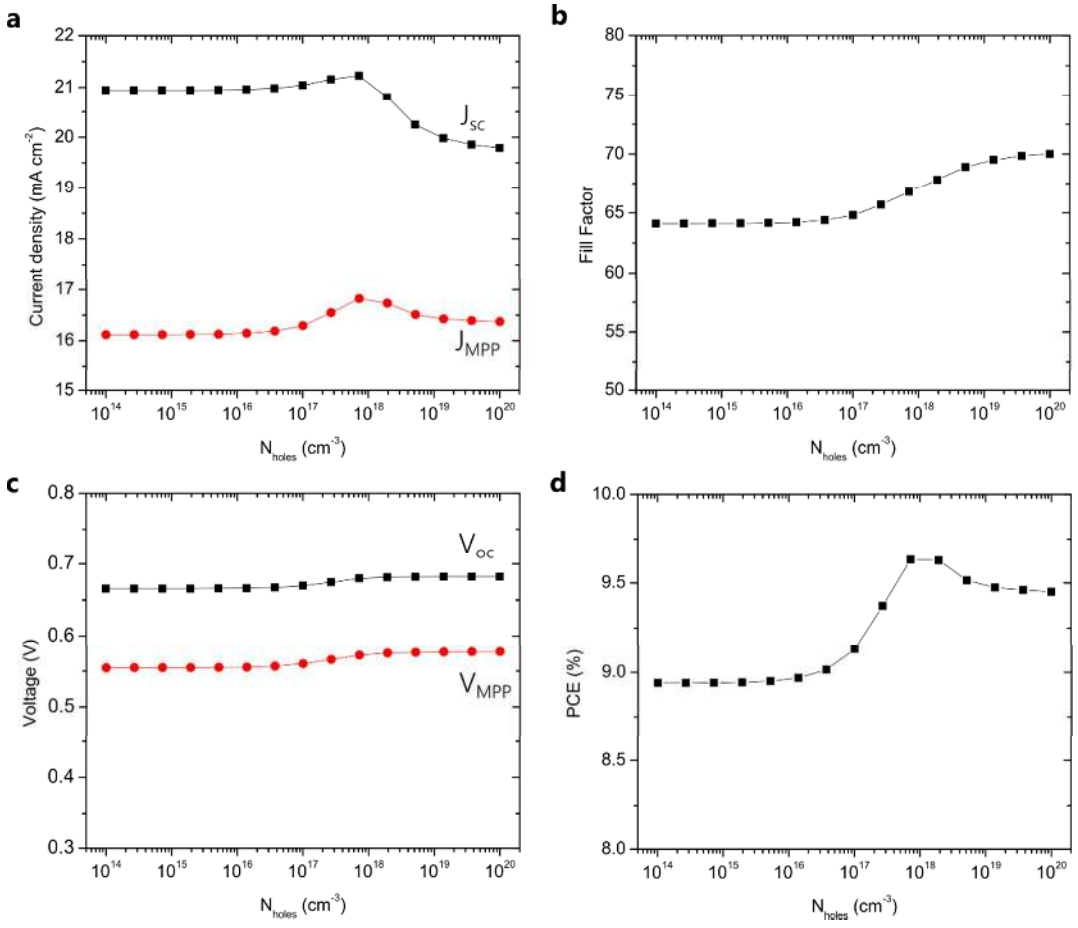

Figure S5. Simulated solar cell parameters as a function of HTL doping concentration.

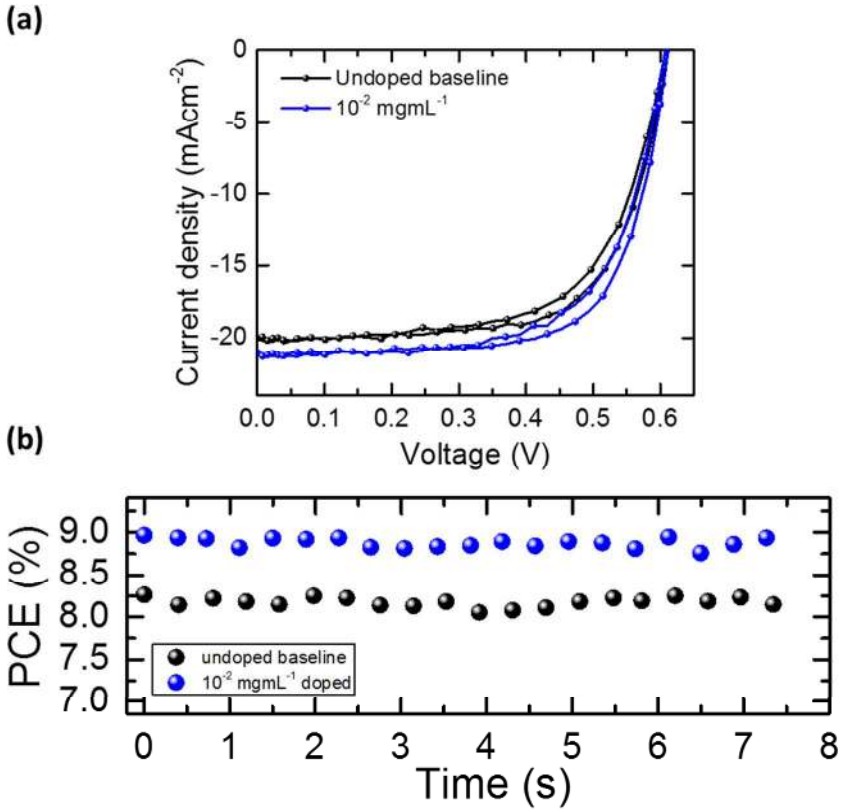

Figure S6. (a) *J-V* curves for $MAPbI_3$-PbS CQD solar cells showing hysteresis. No noticeable increase in hysteresis is detected for the doped cells. (b) Doped cells are found to be stable under light.

Table S1. Summary of the device parameters for the PbX_2-capping based PbS CQD solar cells for the optimized doping condition of 10^{-2} mgmL^{-1}. The reported device parameters (J_{SC}, V_{OC}, FF and PCE) have been averaged over 10 devices. The PCE values in brackets represent the best performing solar cells for each category.

Device	**J_{SC} (mA cm^{-2})**	**V_{OC} (V)**	**FF (%)**	**PCE (%)**
undoped baseline	21.0±1.1	0.61±0.01	65.5±2.5	8.29±0.20 (8.5)
10^{-2} mg mL^{-1}	**22.9±0.5**	**0.59±0.02**	**68.0±1.8**	**9.14±0.18** (9.5)

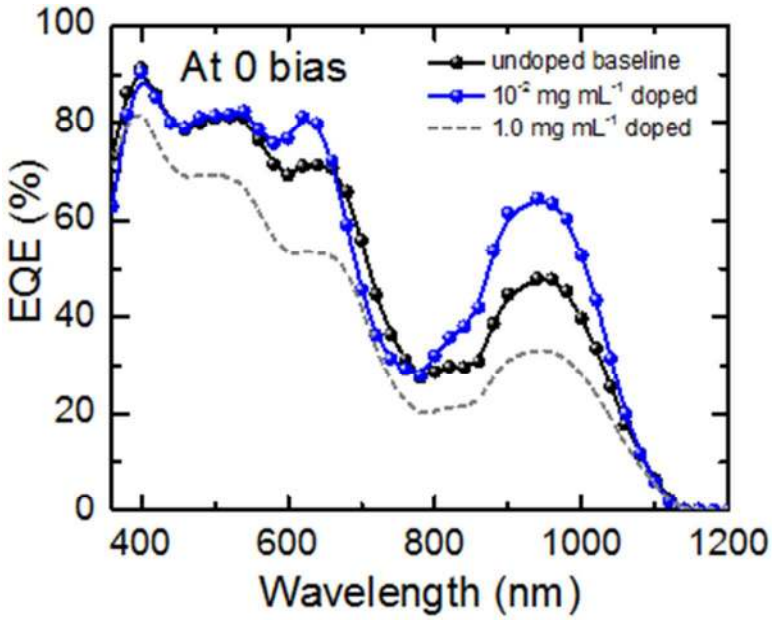

Figure S7. EQE for the $MAPbI_3$-PbS CQD solar cells at 0 bias conditions.

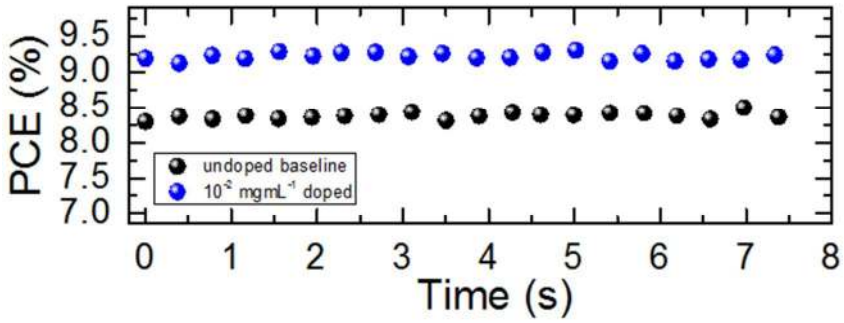

Figure S8. Photostability of the PbX_2-PbS CQD solar cells.

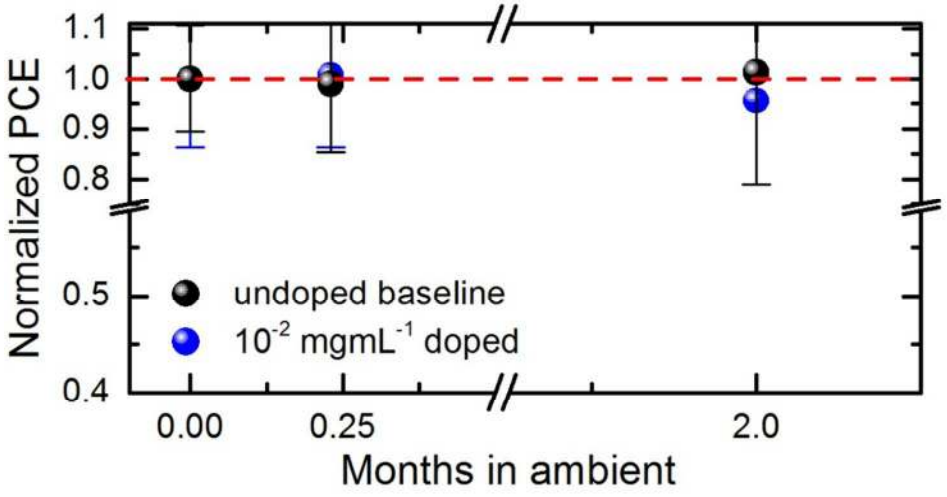

Figure S9. Performance stability of the PbX_2-PbS CQD solar cells is demonstrated.

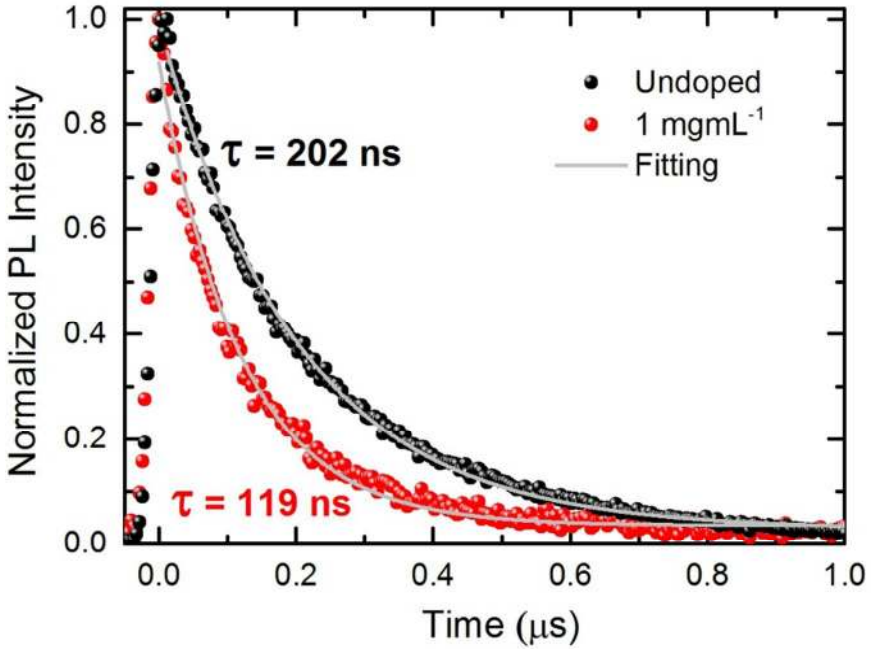

Figure S10. TRPL data for the undoped and doped cases. Doping leads to a reduction in carrier lifetime suggestive of improved hole extraction, in agreement with a recent report.[6]

(1). Ning, Z.; Zhitomirsky, D.; Adinolfi, V.; Sutherland, B.; Xu, J.; Voznyy, O.; Maraghechi, P.; Lan, X.; Hoogland, S.; Ren, Y.*; et al.* Graded Doping for Enhanced Colloidal Quantum Dot Photovoltaics. *Adv. Mater.* **2013,** *25,* 1719-1723.

(2). Yang, Z.; Janmohamed, A.; Lan, X.; García de Arquer, F. P.; Voznyy, O.; Yassitepe, E.; Kim, G.-H.; Ning, Z.; Gong, X.; Comin, R.*; et al.* Colloidal Quantum Dot Photovoltaics Enhanced by Perovskite Shelling. *Nano Lett.* **2015,** *15,* 7539-7543.

(3). Liu, M.; Voznyy, O.; Sabatini, R.; Garcia de Arquer, F. P.; Munir, R.; Balawi, A. H.; Lan, X.; Fan, F.; Walters, G.; Kirmani, A. R.*; et al.* Hybrid Organic-Inorganic Inks Flatten the Energy Landscape in Colloidal Quantum Dot Solids. *Nat. Mater.* **2017,** *16,* 258-263.
(4). Paniagua, S. A.; Baltazar, J.; Sojoudi, H.; Mohapatra, S. K.; Zhang, S.; Henderson, C. L.; Graham, S.; Barlow, S.; Marder, S. R. Production of Heavily n- and p-Doped CVD Graphene with Solution-Processed Redox-Active Metal-Organic Species. *Mater. Horiz.* **2014,** *1,* 111-115.
(5). Burgelman, M.; Decock, K.; Khelifi, S.; Abass, A. Advanced Electrical Simulation of Thin Film Solar Cells. *Thin Solid Films* **2013,** *535,* 296-301.
(6). Liu, D.; Li, Y.; Yuan, J.; Hong, Q.; Shi, G.; Yuan, D.; Wei, J.; Huang, C.; Tang, J.; Fung, M.-K. Improved Performance of Inverted Planar Perovskite Solar Cells with F4-TCNQ Doped PEDOT:PSS Hole Transport Layers. *J. Mater. Chem. A* **2017,** *5,* 5701-5708.